# Polarization-induced photovoltaic effects in Nd-doped BiFeO 3 ferroelectric thin films



doi: 10.1143/JJAP.51.09LE10

# Polarization-Induced Photovoltaic Effects in Nd-Doped $BiFeO_3$ Ferroelectric Thin Films

Yohei Ukai, Shuhei Yamazaki, Takeshi Kawae, and Akiharu Morimoto*

Graduate School of Natural Science and Technology, Kanazawa University, Kanazawa 920-1192, Japan

Nd-doped $BiFeO_3$ (BNF) thin films were fabricated on $SrRuO_3$ (SRO)-coated (100) Nb-doped $SrTiO_3$ substrates by pulsed laser deposition, and nondoped $BiFeO_3$ (BFO) thin films were also fabricated similarly for comparison. Then, Nd-doping effects on ferroelectric and photovoltaic properties were evaluated. Polarization-induced photovoltaic effects were observed in both the BFO and BNF solar cell structures with top and bottom electrodes under intense laser illumination. Using Au top electrodes, enhanced photovoltaic properties were observed in the BNF cell compared with the BFO cell. To improve the photovoltaic properties of the BNF cell, instead of the Au top electrodes, In-Sn-O (ITO) top electrodes were employed for the BNF cell. As a result, the photovoltaic properties were found to be markedly improved, resulting in an open circuit voltage of 0.81 V and a short circuit current density of 12.1 $mA/cm^2$.

* E-mail address: amorimot@ec.t.kanazawa-u.ac.jp

## 1. Introduction

$BiFeO_3$ (BFO) is known to be a Pb-free ferroelectric material with excellent ferroelectric properties comparable to those of $Pb(Zr,Ti)O_3$.[1-3] Large remnant polarizations $P_r$ (above 60 μC/cm$^2$) have been reported for BFO films fabricated by various deposition methods.[4-8] Hence, BFO is expected to be a promising Pb-free ferroelectric material for realizing environment-friendly and highly-integrated ferroelectric random access memories (FeRAMs).[9,10]

On the other hand, as serious problems for the industrial application of FeRAMs using BFO films, there are large leakage currents and large coercive fields $E_c$ (generally, 300-400 kV/cm)[4-8]. Many research groups have reported that a site-engineering technique using various elements is effective to suppress the leakage current in BFO films.[11-16] We proposed (Nd,Mn)-codoped BFO (BNFM) and (Pr,Mn)-codoped BFO (BPFM), and succeeded in obtaining improved electrical properties.[14, 17-18]

Recently, polarization-induced photovoltaic properties in BFO films have been reported.[19-21] The photovoltaic properties are completely different from those of conventional pn and Schottky junctions originating from the built-in-field induced by space charge in depletion layers. Among the ferroelectrics, BFO has the large $P_r$ and a rather small energy gap $E_g$ of 2.67 eV with the direct transition type.[22] The latter feature is expected to have large optical absorption coefficients in the visible light regime and to lead to a promising photovoltaic material with a novel mechanism. In contrast to the ferroelectric applications, the disadvantages of a large leakage current and a large $E_c$ can be turned into be advantages for photovoltaic applications with excellent and stable properties.

As mentioned above, the doping of foreign atoms into BFO is effective for the control of leakage current. The leakage current density in ferroelectrics corresponds to

the dark current density or the dark conductivity in photovoltaics. In this paper, the effect of Nd doping into BFO films on the ferroelectric and photovoltaic properties will be presented. For obtaining favorable properties of BFO films, among the various conductive oxide materials, the pseudo-cubic perovskite $SrRuO_3$ (SRO) with a low resistivity (single crystal: 280 μΩcm) [23-25] was employed as bottom electrodes. Nb-doped (100)STO substrates were used to obtain excellent crystallinity and electrical conduction of the whole structure. As top electrodes, a Au thin film or an In-Sn-O (ITO) thin film was used, resulting in solar cell structures.

## 2. Experimental Procedure

SRO films and BFO or BNF films were deposited on 0.05 wt% Nb-doped (100)$SrTiO_3$ (Nb:STO) substrates using a conventional pulsed laser deposition (PLD) system with a KrF excimer laser (Coherent COMPex102FZ, 248 nm in wavelength). The (100)Nb:STO substrates have a miscut angle of 0˚. Sintered ceramics with compositions of $SrRuO_3$, $Bi_1Fe_1O_3$, $Bi_1Nd_{0.03}Fe_1O_3$, and 10 wt% $SnO_2$-doped $In_2O_3$ were used as targets for SRO, BFO, BNF, and ITO films, respectively. Detailed deposition conditions for SRO, BFO, BNF, and ITO films are summarized in Table I. Before the deposition of SRO films, the Nb:STO substrate was soaked in $NH_4F$-buffered HF solution (BHF) and annealed in air at 1000 ˚C for 60 min.[24,26,27] The thickness of deposited SRO films was 100 nm, and the BFO or BNF film thickness was 170 nm. Au top electrodes with an area of $20 \times 10^{-6}$ $cm^2$ were deposited on the BFO or BNF film by thermal evaporation using a shadow mask to obtain solar cell structures. Instead of the Au top electrodes, ITO top electrodes of $16 \times 10^{-6}$ $cm^2$ in areas were also deposited on the BNF films by PLD.

The crystal structure of the films was determined by X-ray diffraction (XRD; Shimadzu XD-D1) analysis with Cu Kα radiation. The optical absorption spectra were

measured by a conventional spectrometer (JASCO V-570). The electrical properties of cells were examined using a pA meter/DC voltage source (Agilent 4140B) and a ferroelectric test system (Toyo FCE-3). For the characterization of the electrical properties, the current density vs voltage (*J*-*V*) properties were examined with and without laser light illumination. To characterize photovoltaic properties, the illumination using an Ar ion laser (Spectra-Physics Stabilite 2017) with 488 nm line and a power density of 1-3 W/cm$^2$ was carried out. All measurements were performed at room temperature (RT).

## 3. Results and Discussion

XRD θ-2θ scans revealed that both the films were grown with the preferential (*h*00) orientation without any impurity phases or other orientations. The XRD spectra are not shown here.

Figure 1 shows the absorption coefficient α as a function of the photon energy *hν* in the BNF film on a fused quartz substrate. The linear $(\alpha h\nu)^2$ vs *hν* plot in Fig. 1(a) shows a linear relationship above an photon energy of 2.8 eV, suggesting the direct transition type of optical absorption. The linear extrapolation of the high energy spectrum gives us an $E_g$ of 2.71 eV. This value is very close to the reported $E_g$ of 2.67 eV for the BFO film.[22] Figure 1(b) shows a logarithmic plot of the absorption α spectrum. The BNF film shows a large optical absorption α of $5.9 \times 10^4$ cm$^{-1}$ at 2.54 eV even if *hν* is below $E_g$ of 2.71 eV, suggesting that a 170-nm-thick BNF film absorbs more than 50% of the incident Ar ion laser light.

Nondoped BFO films often show large leakage currents and poor hysteresis loops owing to the valence fluctuation of Fe ions and/or Bi or O deficiencies, etc.[14,18,28] In fact, it is not easy to obtain excellent ferroelectric properties of non-doped BFO films reproducibly. The current densities as a function of the applied electric field (*J*-*E*

characteristics) of the BFO and BNF cells with the Au top electrodes are shown in Fig. 2. The BNF cell shows a rather small current density, especially in the small-electric-field regime while the BFO cell shows a large current density. Nd doping seems to reduce the “leakage” current density because Nd will substitute the Bi sites and reduce the Bi deficiency.[14,18)]

Next, the ferroelectric properties of the BFO and BNF cells were investigated. Figure 3 shows the polarization vs the electric field (*P*-*E*) curves of the BFO and BNF cells with a sweep frequency of 20 kHz at RT. Both the cells show ferroelectric behaviors although the hysteresis curves show slightly rounded and open loops, suggesting poor ferroelectric behaviors with large leakage currents. Moreover, the BNF cell shows a larger $E_c$ than the BFO cell. This increase in $E_c$ due to the Nd doping is presumably ascribed to an enhancement of the pinning effect on ferroelectric domains. The BNF cell shows more rounded and poorer loops than the BFO cells, although the former shows the lower current density than the latter, as shown in Fig. 2. It should be noted that the applied electric field for the BNF cell shown in Fig. 2 is limited to ±300 kV/cm while that shown in Fig. 3(b) is expanded to above ±800 kV/cm, which is related to the large $E_c$. The rounded *P*-*E* curves of the BNF cell seem to be caused by larger current densities in the high-electric-field regime, compared with the BFO cell. Nevertheless, from the results of the BFO and BNF cells shown in Fig. 3 it is expected that the voltage sweeps from -4 to +4 V and vice versa switch the ferroelectric polarization.

Then, photoexcited carrier transport and photovoltaic measurements were performed for these cells. Figure 4 shows *J*-*V* curves with and without illumination, denoted by “under ill.” and “dark”, respectively, for the BFO and BNF cells. Before the present photovoltaic measurements, a voltage of ±10 or ±16 V was applied to both the cells under the dark condition, resulting in certain poled states. The forward voltage

sweep is in the direction from minus to plus, and the reverse voltage sweep is in the reverse direction. The voltage sweeps were carried out at swing voltages of ±4 V. The figures shown here are the magnified *J*-*V* curves around the origin. From Figs. 4(a) and 4(b) it was found that these cells show a photovoltaic effect depending on the voltage sweep history, resulting in the finite short circuit current density $J_{sc}$ and open circuit voltage $V_{oc}$. The dark *J*-*V* curve of the BFO cell shows diode-like behavior, and the *J*-*V* curve under illumination shows symmetric photovoltaic behavior with opposite signs of $J_{sc}$ and $V_{oc}$ against the origin, depending on the voltage sweep history (Fig. 4(a)). On the other hand, the dark *J*-*V* curve of the BNF cell (Fig. 4(b)) shows a high resistance state irrespective of the voltage. The *J*-*V* curve of the BNF cell under illumination shows asymmetric photovoltaic behavior against the origin with the same signs of $J_{sc}$ and $V_{oc}$ with a voltage-sweep-dependent hysteresis (Fig. 4(b)). These photovoltaic features are completely different from the conventional features of pn-diode, pin-diode, or Schottky-diode solar cells without any voltage-sweep hystereses. The conventional photovoltaic property is based on the dark diode-like *J*-*V* behavior, and the *J*-*V* curve is shifted downward with an increase in illumination intensity.

The results shown in Figs. 3 and 4 indicate that the present BFO and BNF cells have the polarization-induced photovoltaic effect.[19,21] Generally, the photovoltaic cells with ferroelectrics have two components, the switchable and unswitchable components, which originate from a polarization-induced field and a stable built-in field such as the Schottky barrier, respectively, as follows:[29]

$$\left|V_{oc}^{p}\right| = \frac{V_{oc}^{F} - V_{oc}^{R}}{2}, \qquad \left|V_{oc}^{bi}\right| = \frac{V_{oc}^{F} + V_{oc}^{R}}{2}, \qquad (1)$$

$$\left|J_{sc}^{p}\right| = \frac{J_{sc}^{F} - J_{sc}^{R}}{2}, \qquad \left|J_{sc}^{bi}\right| = \frac{J_{sc}^{F} + J_{sc}^{R}}{2}. \qquad (2)$$

In eq. (1), $V_{oc}^{F}$ and $V_{oc}^{R}$ are the measured $V_{oc}$ with the forward sweep and reverse

sweep, respectively, and $V_{oc}^{p}$ and $V_{oc}^{bi}$ are the polarization-induced and built-in $V_{oc}$, respectively. In eq. (2), $J_{sc}^{F}$ and $J_{sc}^{R}$ are the measured $J_{sc}$ with the forward sweep and reverse sweep, respectively, and $J_{sc}^{p}$ and $J_{sc}^{bi}$ are the polarization-induced and built-in $J_{sc}$, respectively. From this viewpoint, the BNF cell is found to have two aforementioned components while the BFO cell mainly has the switchable component. To improve the resultant photovoltaic properties, the synergistic effect of the polarization-induced (switchable) and built-in (unswitchable) fields with the same direction is expected. Unfortunately, a detailed relationship between the dark *J*-*V* properties and the photovoltaic properties has not been clarified yet.

On the other hand, so far, two models have been proposed for the switchable polarization-induced photovoltaic effect. Yang *et al*. reported that a high-quality BFO film with coplanar electrodes shows an “above-band gap” photovoltage proportional to the number of domains, and proposed that the photoexcited carriers are separated at nanoscale steps of the electrostatic potential at ferroelectric domain walls.[21] Lee *et al*. reported that an epitaxial BFO cell sandwiched by top and bottom electrodes shows a “below-band gap” photovoltage, and they proposed that the photoexcited carriers are separated by macroscopic polarization over the whole thickness region.[30] The latter mechanism can be ascribed to the depolarization field, which results from the incomplete screening of ferroelectric polarization by the eletrodes.[29,31] A simple consideration on the polarity of the photovoltaic effect will tell us which mechanism is valid.

Confirmation of the polarity of $V_{oc}$ and $J_{sc}$ of the present cells after the application of the electric field revealed that the present photovoltaic effect is ascribed to the depolarization effect due to the incomplete screening. If a ferroelectric film is sufficiently thick and the conductivity of the metal electrodes employed is high, the

depolarization field will vanish owing to a perfect screening effect. The depolarization field, however, remains at a certain value if the film is sufficiently thin and the metal electrodes have a limited conductivity.[32)]

For comparison between the two cells, the photovoltaic properties with the reverse voltage sweeps are shown again in Fig. 5. The photovoltaic data shown in Fig. 5 are summarized in Table II. The open circuit voltage $V_{oc}$ of the BNF cell with the Au top electrode becomes larger than that of the BFO cell with the Au top electrode while the values of $J_{sc}$ of the two cells are almost the same. Furthermore, the fill factor (FF) of the BNF cell is larger than that of the BFO cell. As a result, the maximum output power $|J_{max} \times V_{max}|$ of the BNF cell is 0.11 [mW/cm$^2$], which is larger than 0.067 [mW/cm$^2$] of the BFO cell.

To improve the photovoltaic property of the BNF cell, the Au top electrode was changed to the ITO top electrode. Figure 6(a) shows the transmittance spectra of the Au and ITO films on the fused quartz substrates. Each film was deposited with the same thickness as that of the top electrode film in the BNF cell shown in Fig. 6(b). The transmittance of the ITO film is improved by a factor of four compared with that of the Au film. Figure 6(b) shows the photovoltaic properties of the BNF cells with the Au or ITO top electrode. Similarly to the measurements shown in Figs. 4(a) and 4(b), before the present photovoltaic measurements, a voltage of $\pm$10 or $\pm$16 V was applied to both of the cells under the dark condition, resulting in certain poled states. The $V_{oc}$ of the BNF cell with the ITO top electrode is markedly increases up by a factor of two to 0.81 V, and the $J_{sc}$ of the BNF cell also increases by a factor of 18 to 12.1 mA/cm$^2$, compared with those of the BNF cell with the Au top electrode. As a result, the maximum output power $|J_{max} \times V_{max}|$ of the BNF cell with the ITO top electrode is 4.01 [mW/cm$^2$], which is far larger than 0.11 [mW/cm$^2$] of the BNF cell with the Au top electrode, resulting in a marked increase by a factor of 36. The marked improvement of

the photovoltaic properties cannot be solely ascribed to the improvement of the transmittance of the ITO electrode by a factor of four. Chen *et al*. also reported that the photovoltaic response of a BFO cell with an ITO top electrode is about 25 times higher than that with a Au top electrode.[33] Qin *et al*. proposed that the origin of the improvement of the photovoltaic properties in a (Pb,La)(Zr,Ti)$O_3$ ferroelectric film with a conductive oxide top electrode is the reduced screening effect due to the high dielectric constant of the top electrode.[34]

The depolarization field $E_{dep}^{p}$ in the ferroelectric film is known to be governed by the following equation:

$$E_{dep}^{p} = \frac{V_{FE}^{p}}{l} = -\frac{P}{\varepsilon_{FE}} \frac{\frac{2\varepsilon_{FE}}{l}}{\frac{2\varepsilon_{FE}}{l} + \frac{\varepsilon_e}{l_s}}, \qquad (3)$$

where $V_{FE}^{p}$ is the voltage, *P* is the polarization, $\varepsilon_{FE}$ is the dielectric constant, and $l$ is the thickness of the ferroelectric film. Moreover, $\varepsilon_e$ is the dielectric constant, and $l_s$ is the screening length of the electrode.[32] On the basis of eq. (3) it can be considered that the depolarization field $E_{dep}^{p}$ is affected by the metal screening length $l_s$ as well as the metal dielectric constant $\varepsilon_e$. For estimating a plausible $E_{dep}^{p}$ an appropriate metal dielectric constant should be used. However, it is difficult to estimate an appropriate $\varepsilon_e$. Therefore, we primarily attribute the origin of the present marked improvement of the photovoltaic property of the cell with the ITO top electrode to the larger screening length $l_s$ of the ITO electrode owing to the rather small carrier density of the ITO electrode deposited at RT compared with that of the Au electrode.

## 4. Conclusions

Polarization-induced photovoltaic effects were observed in both the BFO and BNF solar

cell structures with the top and bottom electrodes under intense laser illumination. Using Au top electrodes, enhanced photovoltaic properties were observed in the BNF cell compared with the BFO cell. To improve the photovoltaic properties of the BNF cell, instead of the Au top electrodes, ITO electrodes were employed. As a result, the photovoltaic properties of the BNF cell were found to be markedly improved, resulting in an open circuit voltage of 0.81 V and a short circuit current density of 12.1 $mA/cm^2$.

**Acknowledgements**

The authors would like to thank Y. Nomura for his technical support in some experiments. This work was supported in part by a Grant-in-Aid for Challenging Exploratory Research (No. 23656212) from the Japan Society for the Promotion of Science (JSPS).

1) J. Wang, J. B. Neaton, H. Zheng, V. Nagarajan, S. B. Ogale, B. Liu, D. Viehland, V. Vaithyanathan, D. G. Schlom, U. V. Waghmare, N. A. Spaldin, K. M. Rabe, M. Wuttig, and R. Ramesh: Science **299** (2003) 1719.

2) J. Wang, H. Zheng, Z. Ma, S. Prasertchoug, M. Wuttig, R. Droopad, J. Yu, K. Eisenbeiser, and R. Ramesh: Appl. Phys. Lett. **85** (2004) 2574.

3) D. Lebeugle, D. Colson, A. Forget, and M. Viret: Appl. Phys. Lett. **91** (2007) 022907.

4) K. Y. Yun, D. Ricinschi, T. Kanashima, and M. Okuyama: Appl. Phys. Lett. **89** (2006) 192902.

5) J. Li, J. Wang, M. Wuttig, R. Ramesh, N. Wang, B. Ruette, A. P. Pyatakov, A. K. Zvezdin, and D. Viehland: Appl. Phys. Lett. **84** (2004) 5261.

6) S. Y. Yang, F. Zavaliche, L. M. Ardabili, V. Vaithyanathan, D. G. Schlom, Y. J. Lee, Y. H. Chu, M. P. Cruz, Q. Zhan, T. Zhao, and R. Ramesh: Appl. Phys. Lett. **87** (2005) 102903.

7) A. Z. Simoes, L. S. Cavalcante, C. S. Riccardi, J. A. Varela, and E. Longo: Curr. Appl. Phys. **9** (2009) 520.

8) K. Sone, H. Naganuma, T. Miyazaki, T. Nakajima, and S. Okamura: Jpn. J. Appl. Phys. **49** (2010) 09MB03.

9) Z. Zhong, S. K. Singh, K. Maruyama, and H. Ishiwara: Jpn. J. Appl. Phys. **47** (2008) 2230.

10) Y. Wang, R. Y. Zheng, C. H. Sim, and J. Wang: J. Appl. Phys. **105** (2009) 016106.

11) H. Uchida, R. Ueno, H, Funakubo, and S. Koda: J. Appl. Phys. **100** (2006) 014106.

12) H. Naganuma, J. Miura, and S. Okamura: Appl. Phys. Lett. **93** (2008) 052901.

13) B. Yu, M. Li, Z. Hu, L. Pei, D. Guo, X. Zhao, and S. Dong: Appl. Phys. Lett. **93** (2008) 182909.

14) T. Kawae, H. Tsuda, H. Naganuma, S. Yamada, M. Kumeda, S. Okamura, and A. Morimoto: Jpn. J. Appl. Phys. **47** (2008) 7586.

15) J. M. Park, S. Nakashima, F. Gotoda, T. Kanashima, and M. Okuyama: Jpn. J. Appl. Phys. **48** (2009) 09KB03.

16) T. Kawae, Y. Terauchi, H. Tsuda, M. Kumeda, and A. Morimoto: Appl. Phys. Lett. **94** (2009) 112904.

17) T. Kawae, Y. Terauchi, T. Nakajima, S. Okamura, and A. Morimoto: J. Ceram. Soc. Jpn. **118** (2010) 652.

18) T. Kawae, H. Tsuda, and A. Morimoto: Appl. Phys. Express **1** (2008) 051601.

19) S. Y. Yang, L. W. Martin, S. J. Byrnes, T. E. Conry, S. R. Basu, D. Paran, L. Reichertz, J. Ihlefeld, C. Adamo, A. Melville, Y.-H. Chu, C.-H. Yang, J. L. Musfeldt, D. G. Schlom, J. W. Ager III, and R. Ramesh: Appl. Phys. Lett. **95** (2009) 062909.

20) T. Choi, S. Lee, Y. J. Choi, V. Kiryukhin, and S.-W. Cheong: Science **324** (2009) 63.

21) S. Y. Yang, J. Seidel, S. J. Byrnes, P. Shafer, C.-H. Yang, M. D. Rossell, P. Yu, Y.-H. Chu, J. F. Scott, J. W. Ager, III, L. W. Martin, and R. Ramesh: Nat. Nanotechnol. **5** (2010) 143.

22) S. R. Basu, L. W. Martin, Y. H. Chu, M. Gajek, R. Ramesh, R. C. Rai, X. Xu, and J. L. Musfeldt: Appl. Phys. Lett. **92** (2008) 091905.

23) C. B. Eom, R. J. Cava, R. M. Fleming, J. M. Philips, R. B. Dover, J. H. Marshall, J. W. P. Hsu, J. J. Krajewski, and W. F. Peck, Jr.: Science **258** (1992) 1766.

24) R. A. Rao, Q. Gan, and C. B. Eom: Appl. Phys. Lett. **71** (1997) 1171.

25) T. Kamo, K. Nishida, K. Akiyama, J. Sakai, T. Katoda, and H. Funakubo: Jpn. J. Appl. Phys. **46** (2007) 6987.

26) H. Fujisawa, Y. Seioh, M. Kume, and M. Shimizu: Jpn. J. Appl. Phys. **47** (2008) 7505.

27) T. Kawae, Y. Tsukada, Y. Terauchi, T. Nakajima, Y. Nomura, S. Okamura, and A. Morimoto: Jpn J. Appl. Phys. **50** (2011) 09NA09.

28) S. K. Singh and H. Ishiwara: Jpn. J. Appl. Phys. **44** (2005) L 734.

29) W. Ji, K. Yao, and Y. C. Liang: Adv. Mater. **22** (2010) 1763.

30) D. Lee, S. H. Baek, T. H. Kim, J.-G. Yoon, C. M. Folkman, C. B. Eom, and T. W. Noh: Phys. Rev. B **84** (2011) 125305.

31) J. Junquera and P. Ghosez: Nature **422** (2003) 506.

32) R. R. Mehta, B. D. Silverman, and J. T. Jacobs: J. Appl. Phys. **44** (1973) 3379.

33) B. Chen, M. Li, Y. Liu, Z. Zuo, F. Zhuge, Q.-F. Zhan, and R.-W. Li: Nanotechnology **22** (2011) 195201.

34) M. Qin, K. Yao, and Y. C. Liang: Appl. Phys. Lett. **95** (2009) 022912.

**Figure Captions**

Fig. 1. (Color online) Absorption coefficient α as a function of the photon energy $h\nu$ in the BNF film. (a) Linear $(\alpha h\nu)^2$ vs $h\nu$ plot for direct transition type and (b) log α vs $h\nu$ plot.

Fig. 2. (Color online) *J-E* curves for the BNF and BFO cells with Au top electrodes.

Fig. 3. (Color online) *P-E* loops in the (a) BFO and (b) BNF cells with Au top electrodes. The hysteresis loops were measured at RT with a measurement frequency of 20 kHz.

Fig. 4. (Color online) *J-V* curves with and without illumination, denoted by "under Ill." and "dark", respectively, in the (a) BFO and (b) BNF cells with Au top electrodes. The forward voltage sweep represents the direction from minus to plus, and the reverse voltage sweep represents the reverse direction.

Fig. 5. (Color online) *J-V* curves with the reverse sweep under illumination in the BFO (black dashed-dotted curve) and BNF (red broken curve) cells with Au top electrodes. $J_{max}$ and $V_{max}$ represent the current density and the voltage with the maximum output $|J_{max} \times V_{max}|$, respectively.

Fig. 6. (Color online) Influence of the top electrode. (a) Transmittance spectra in Au (black broken curve) and ITO (red solid curve) films and (b) *J-V* curves of the cells with Au (black broken curve) and ITO (red solid curve) top electrodes.

Table I. PLD conditions of SRO, BFO, BNF, and ITO films.

| | SRO | BFO, BNF | ITO |
|---|---|---|---|
| Laser energy (mJ) | 120 | 100 | 100 |
| Repetition rate (Hz) | 2 | 5 | 5 |
| Substrate temperature (˚C) | 700 | 575 | RT |
| $O_2$ pressure during deposition (Pa) | 13.3 | 13.3 | 1.33 |
| $O_2$ pressure during cooling (Pa) | 1330 | 1330 | - |

Table II. Photovoltaic properties of the BFO and BNF cells.

| Ferroelectric film | BFO | BNF | BNF |
|---|---|---|---|
| Top electrode | Au | Au | ITO |
| Short circuit current density $J_{sc}$ (mA/cm$^2$) | -0.69 | -0.66 | -12.1 |
| Open circuit voltage $V_{oc}$ (V) | 0.36 | 0.46 | 0.81 |
| $\lvert J_{sc} \times V_{oc} \rvert$(mW/cm$^2$) | 0.25 | 0.3 | 9.8 |
| Fill factor *FF* | 0.26 | 0.36 | 0.41 |
| $\lvert J_{max} \times V_{max} \rvert$(mW/cm$^2$) | 0.067 | 0.11 | 4.01 |

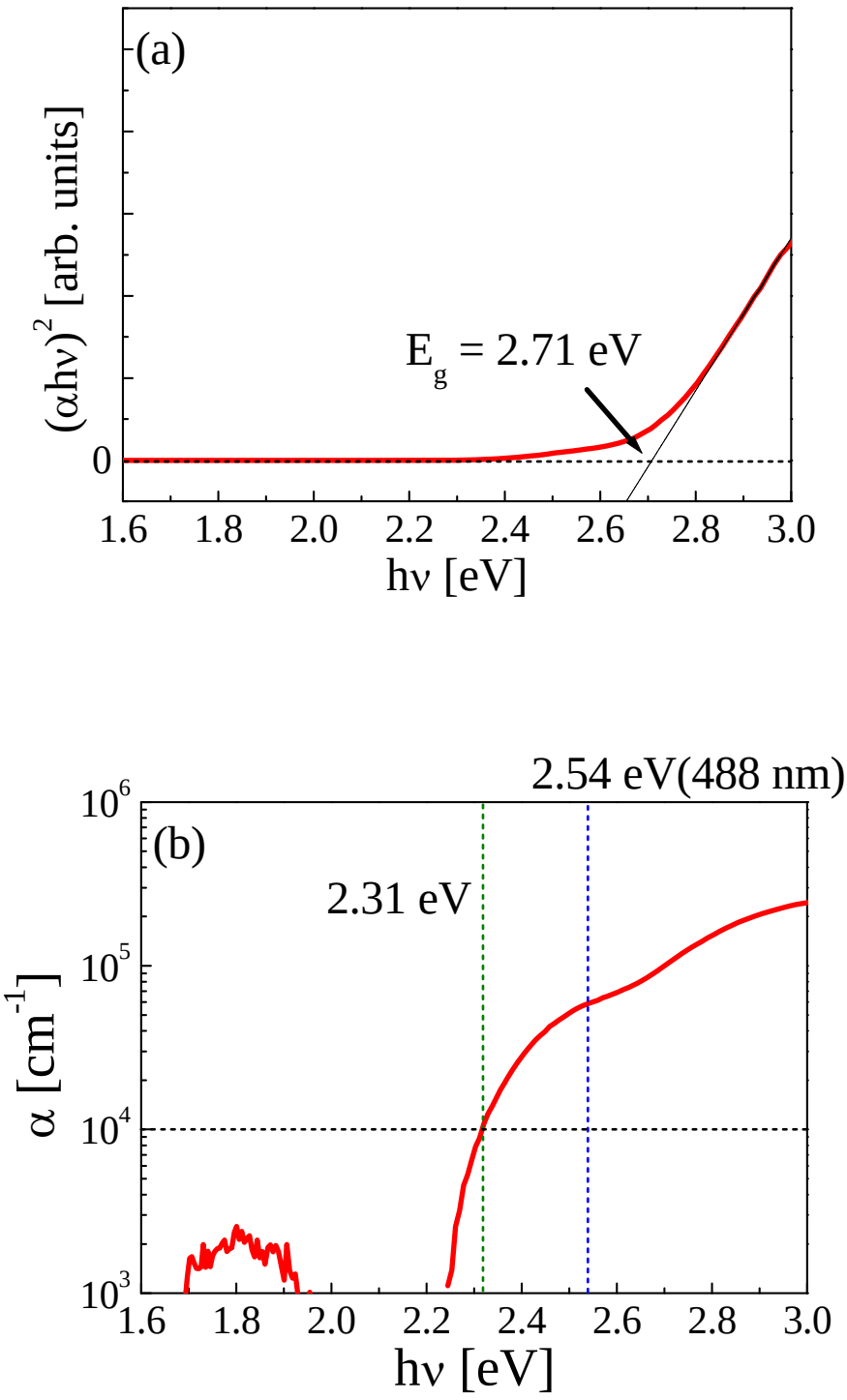
(a)
$(\alpha h\nu)^2$ [arb. units]
$E_g$ = 2.71 eV
0
1.6
1.8
2.0
2.2
2.4
2.6
2.8
3.0
hν [eV]
2.54 eV(488 nm)
(b)
2.31 eV
$10^6$
$10^5$
$10^4$
$10^3$
α [$cm^{-1}$]
1.6
1.8
2.0
2.2
2.4
2.6
2.8
3.0
hν [eV]

Figure 1

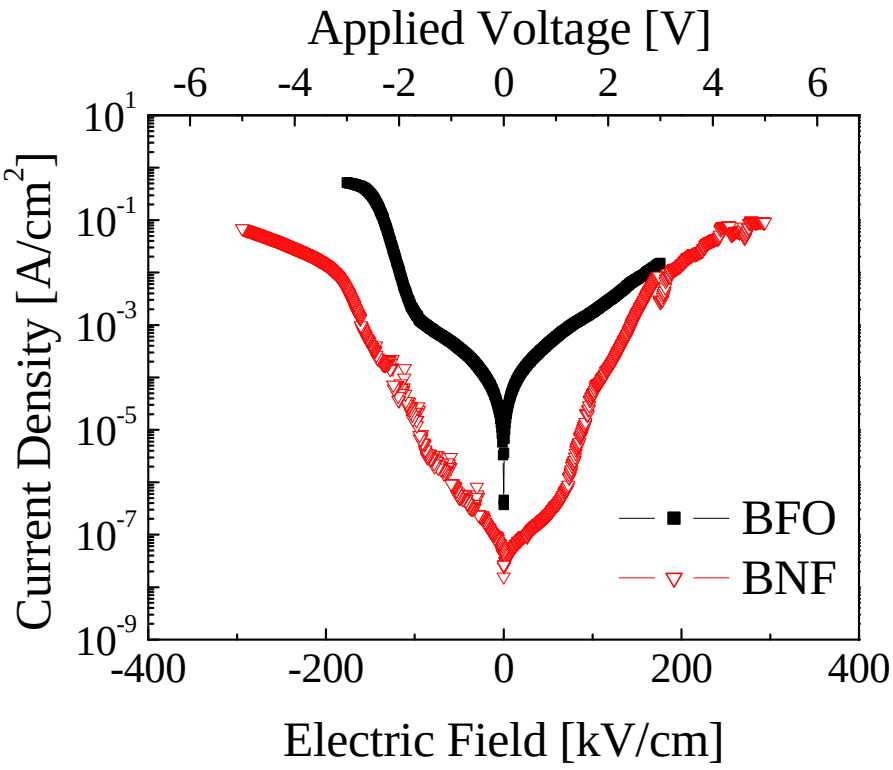
Applied Voltage [V]
-6
-4
-2
0
2
4
6
Current Density [A/cm$^2$]
$10^{1}$
$10^{-1}$
$10^{-3}$
$10^{-5}$
$10^{-7}$
$10^{-9}$
-400
-200
0
200
400
Electric Field [kV/cm]
BFO
BNF

Figure 2

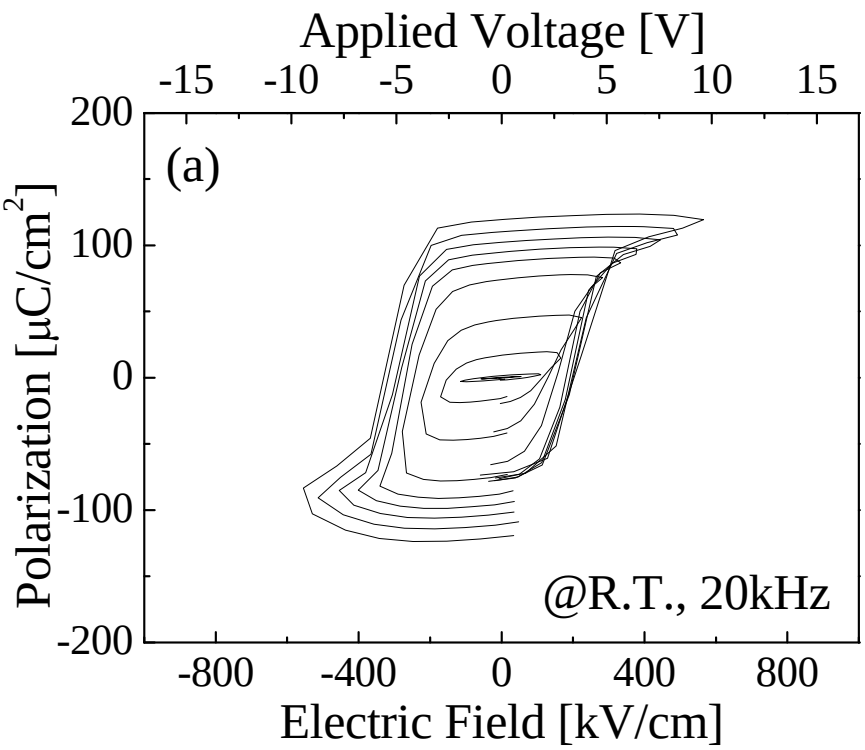
Applied Voltage [V]
-15
-10
-5
0
5
10
15
200
100
0
-100
-200
(a)
Polarization [μC/cm2]
@R.T., 20kHz
-800
-400
0
400
800
Electric Field [kV/cm]

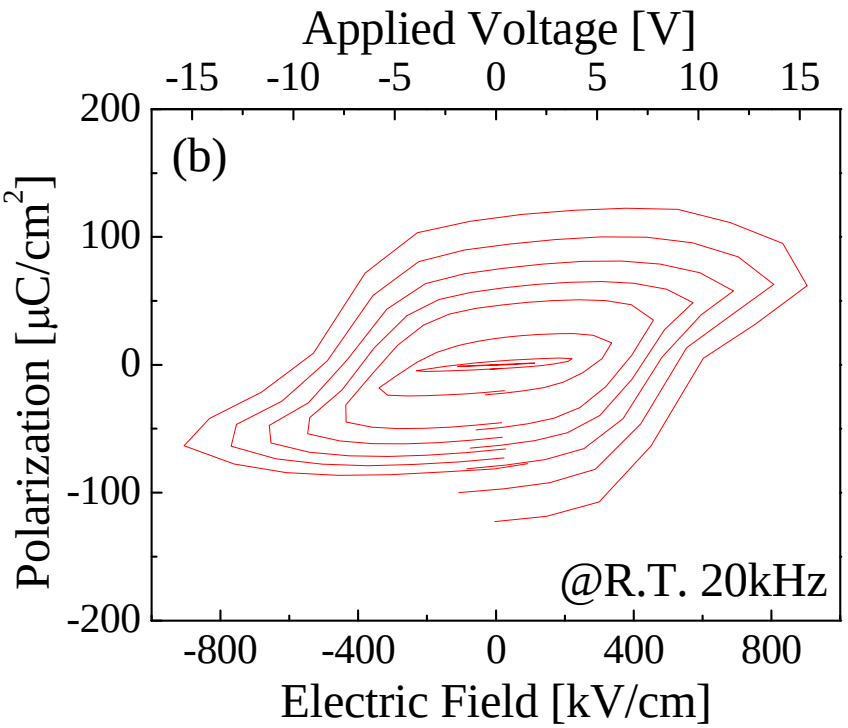
Applied Voltage [V]
-15
-10
-5
0
5
10
15
200
100
0
-100
-200
(b)
Polarization [μC/cm2]
@R.T. 20kHz
-800
-400
0
400
800
Electric Field [kV/cm]

Figure 3

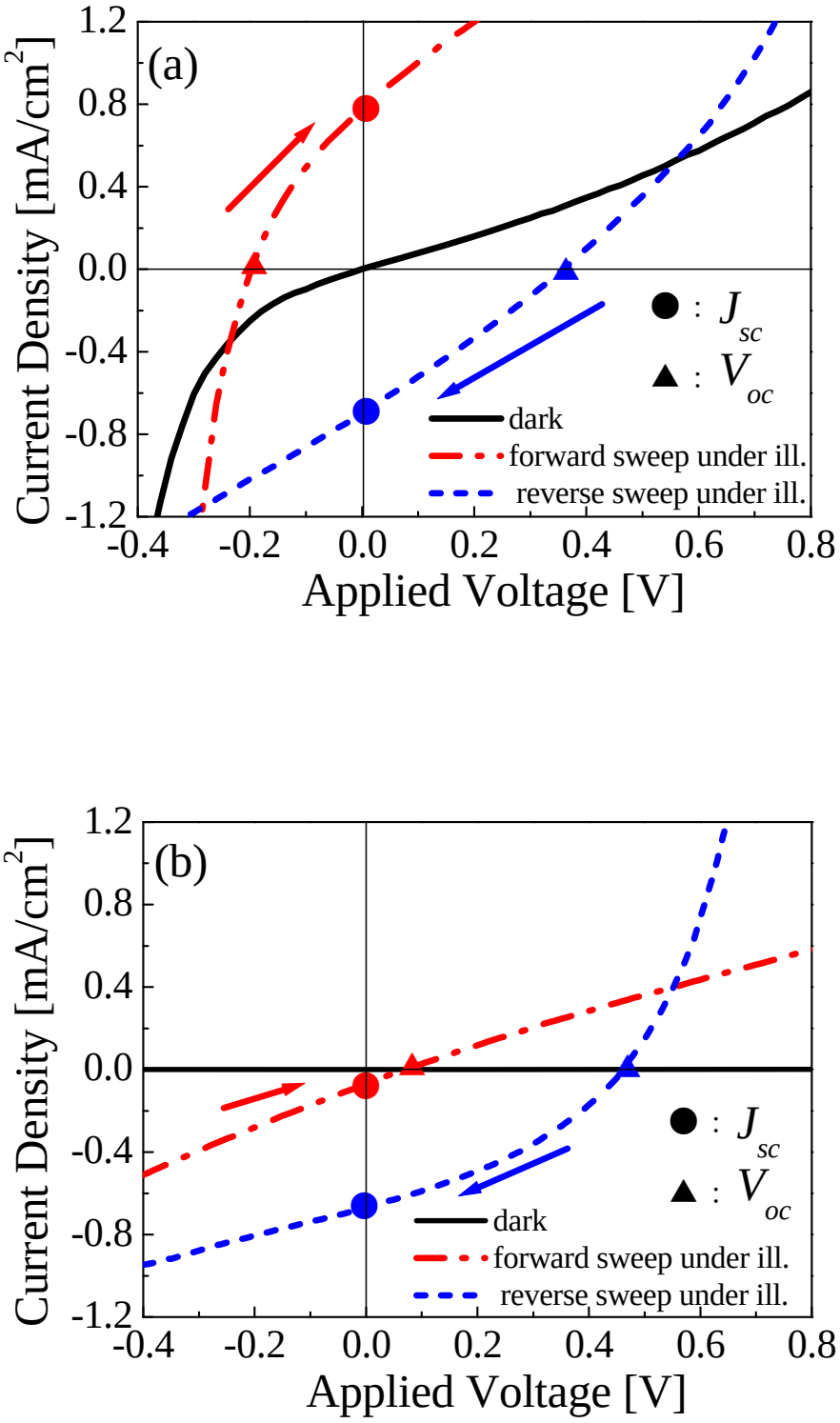
(a)
Current Density [mA/cm$^2$]
Applied Voltage [V]
1.2
0.8
0.4
0.0
-0.4
-0.8
-1.2
-0.4
-0.2
0.0
0.2
0.4
0.6
0.8
● : $J_{sc}$
▲ : $V_{oc}$
dark
forward sweep under ill.
reverse sweep under ill.
(b)
Current Density [mA/cm$^2$]
Applied Voltage [V]
1.2
0.8
0.4
0.0
-0.4
-0.8
-1.2
-0.4
-0.2
0.0
0.2
0.4
0.6
0.8
● : $J_{sc}$
▲ : $V_{oc}$
dark
forward sweep under ill.
reverse sweep under ill.

Figure 4

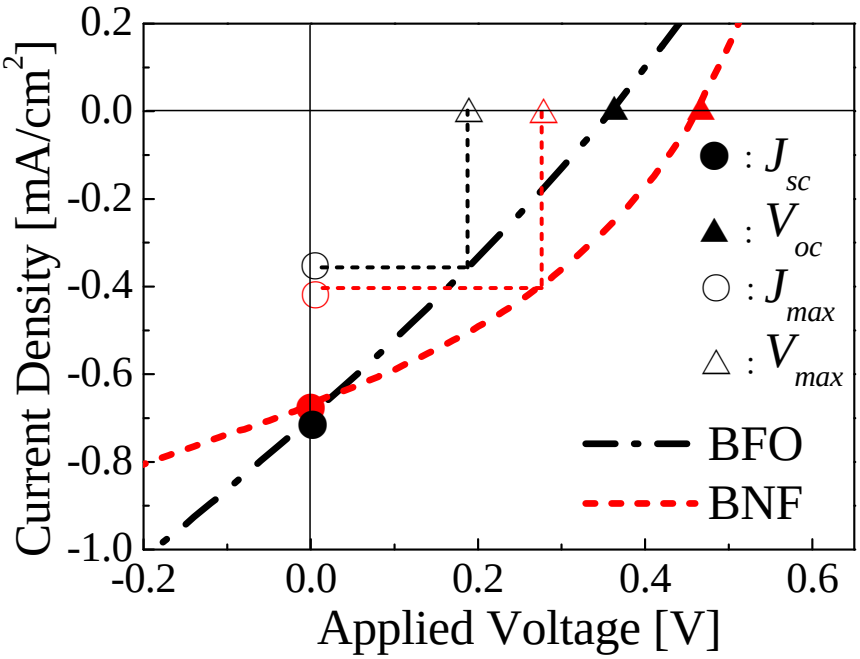
Current Density [mA/cm$^2$]
Applied Voltage [V]
0.2
0.0
-0.2
-0.4
-0.6
-0.8
-1.0
-0.2
0.0
0.2
0.4
0.6
: $J_{sc}$
: $V_{oc}$
: $J_{max}$
: $V_{max}$
BFO
BNF

Figure 5

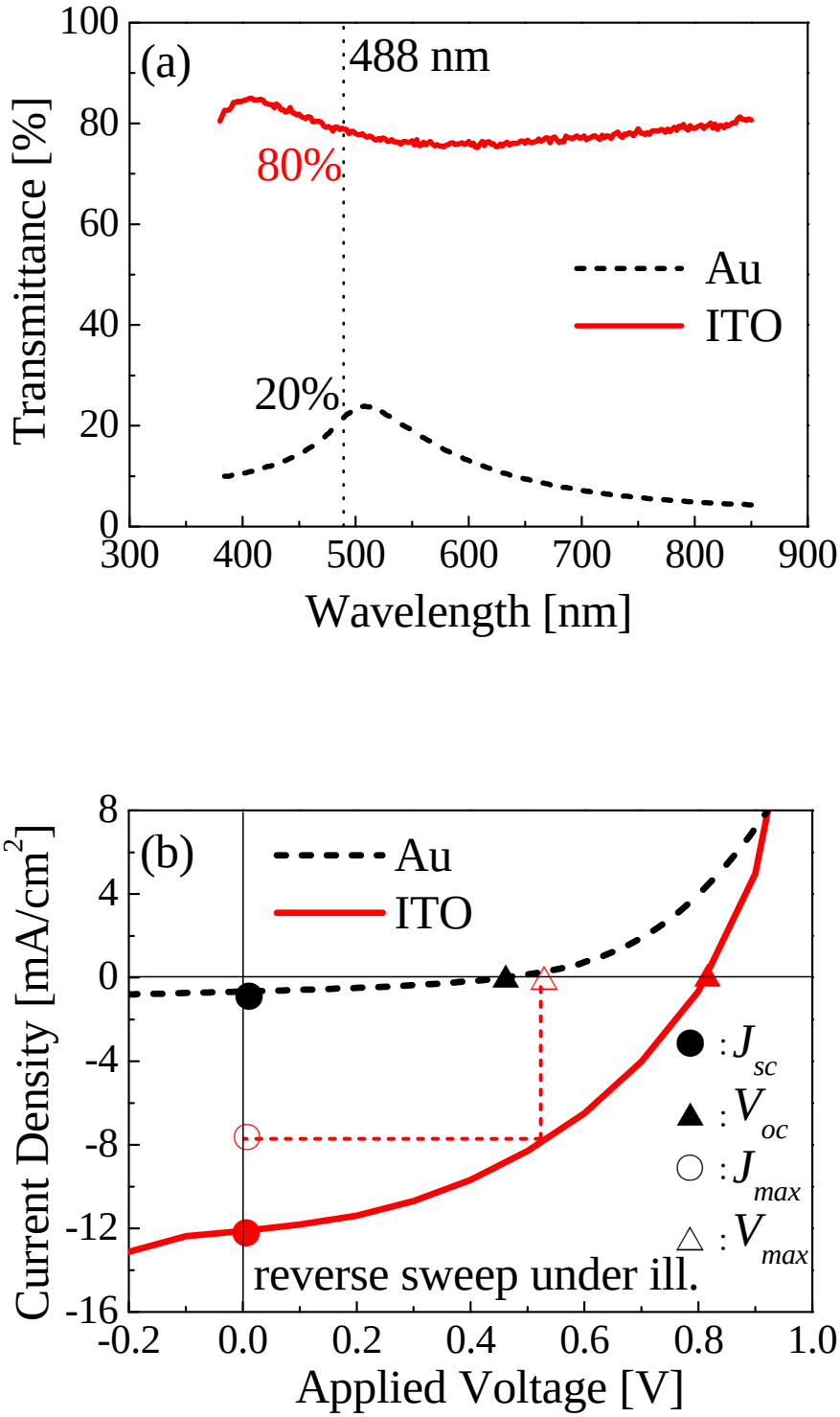
(a)
488 nm
80%
20%
Au
ITO
Transmittance [%]
Wavelength [nm]
100
80
60
40
20
0
300
400
500
600
700
800
900
(b)
Au
ITO
: $J_{sc}$
: $V_{oc}$
: $J_{max}$
: $V_{max}$
reverse sweep under ill.
Current Density [mA/cm$^2$]
Applied Voltage [V]
8
4
0
-4
-8
-12
-16
-0.2
0.0
0.2
0.4
0.6
0.8
1.0

Figure 6